Design and Analysis of a Linear Permanent-Magnet Vernier Machine With Improved Force Density

Wenxiang Zhao, *Senior Member, IEEE*, Junqiang Zheng, Jiabin Wang, *Senior Member, IEEE*, Guohai Liu, *Senior Member, IEEE*, Jianxing Zhao, and Zhuoya Fang

Abstract—**This paper proposes a novel linear permanent-magnet (PM) vernier machine, which offers high force density, high efficiency, simple structure, and low cost. The novelty of the proposed machine is substantiated by integrating appropriate magnetization directions of PMs in the armature core. First, the structure and the operation principle of the proposed machine are descried. The machine is subsequently designed for a given set of specifications and its electromagnetic performances are analyzed by time-stepped transient finite-element method. An analytical equation is derived for evaluation of the thrust force ripple. Finally, experiments on a prototype of the proposed machine are carried out for validation.**

Index Terms—**Electromagnetic analysis, electromagnetic forces, finite-element analysis, harmonic analysis, inductance, magnetic flux leakage, modeling, permanent-magnet (PM) machine.**

NOMENCLATURE

A_s	Electrical loading (A/m).
$B_{e\delta}$	Peak value of flux density of effective harmonic magnetic (T).
c_s	Pole arc coefficient of stator teeth.
E	Phase back-EMF (V).
F_{av}	Average thrust force (N).
F_{detent}	Detent force (N).
F_{ele}	Electromagnetic force (N).
F_{max}	Maximum thrust force (N).
F_{min}	Minimum thrust force (N).
F_n	Nth-order current linkage harmonic (A t).
F_{ra}, F_{rb}, F_{rc}	Fluctuating forces of phases A, B and C, N.
F_{out}	Output thrust force (N).
G_r	Magnetic gear ratio.
G	Air-gap length (mm).
h_{st}	Stator tooth height (mm).
h_{sy}	Stator yoke height (mm).
h_{P0}	PMs thickness (mm).
I	Current (A).
J	Current density (A/mm^2).
K	1, 2, 3, ..., ∞.
k_d	Leakage coefficient.
k_p	Ratio of PMs width-to-stator tooth tip width.
k_{PM}	Ratio of PMs width-to-mover pole pitch.
k_h	Ratio of horizontally magnetized PM width-to-mover spilt slot width.
k_v	Ratio of vertically magnetized PM width-to-mover spilt slot width.
l_m	Mover width (mm).
l_a	Mover length (mm).
L	Phase inductance (mH).
L_0	DC components of self-inductance (mH).
L_{max}	Maximum self-inductance (mH).
M	Motor phase number.
M_0	DC components of mutual inductance (mH).
M_{max}	Maximum mutual inductance (mH).
M_{cu}	Copper mass (kg).
n	1, 3, 5, ..., ∞.
n_s	Active number of the stator teeth within mover length.
n_w	Number of pole pairs of armature winding.
n_a	Number of teeth of armature winding.
N_{ph}	Number of turns per phase.
p_{PM}	Effective number of PM pole pairs.
P_{em}	Electromagnetic power (W).
$P_{n,k}$	Number of pole pairs.
T	Time (s).
V	Mover velocity (m/s).
v_w	Travelling speed of armature magnetic field (m/s).
w_{m0}	Mover slot opening width (mm).
w_{ms}	Split tooth width (mm).
w_{sr}	Stator tooth root width (mm).
w_{st}	Stator tooth width (mm).
w_v	Vertically magnetized PMs width (mm).

W. Zhao, J. Zheng, and G. Liu are with the School of Electrical and Information Engineering, Jiangsu University, Zhenjiang 212013, China (e-mail: zwx@ujs.edu.cn).

J. Wang is with the Department of Electronic and Electrical Engineering, The University of Sheffield, Sheffield S1 3JD, U.K.

J. Zhao is with the China Shipbuilding Industry Corporation, Shanghai 201108, China.

Z. Fang is with the Basic Engineering Training Center, Jiangsu University, Zhenjiang 212013, China.

w_h	Horizontally magnetized PMs width (mm).
w_p	Mover spilt slot width (mm).
x	Mover position (mm).
x_0	Initial position of mover (mm).
x_1, x_2, x_3	Initial displacement between current and inductance (mm).
τ_m	Mover pole pitch (mm).
τ_s	Stator tooth pitch (mm).
Λ_0	DC component in permeance function (H/m^2).
Λ_k	Amplitude of kth-order harmonic (H/m^2).
ψ	Flux linkage (Wb).
ψ_{PM}	PM flux linkage (Wb).

Fig. 1. Schematics of existing and proposed PM arrays for high-force density vernier machines.

Fig. 2. Proposed LPMV machine.

I. Introduction

NOWADAYS, permanent-magnet (PM) machines have received increased attention in many transportation applications [1]–[3]. Compared with traction systems based on conventional rotary machines, urban rail transit systems employing linear drive eliminate costly and bulky rotary-to-linear transmissions. Consequently, system performance can be improved and system size reduced [4].

For a variety of linear drive applications, high force density is essential. A coaxial magnetic gear has been proposed, which offers high torque density [5]–[7]. By extending this idea to linear topology and integration of a linear magnetic gear with a linear machine, both high force density and high efficiency can be achieved [8], [9]. However, the integrated machines employ two or more moving parts with multiple air-gaps; thus, they suffer from manufacture difficulty. To circumvent this problem, a new class of linear machines based on the field modulation principle of the magnetic gear, known as vernier machines, was introduced [10]. This vernier machine with one air-gap offers simpler structure than the magnetic geared machine. For conventional linear PM machines with long stroke such as rail transit, the system will suffer from high cost if PMs or windings are located on the long stator [11]. Thus, the challenge is how to realize the merits of high efficiency and high force density with low cost for long-stroke PM linear machines.

Recently, rotary stator-PM machines and linear primary-PM vernier machines were proposed [12]–[18]. Since both magnets and coils are mounted on either stator or mover, the problems of excessive use of PMs or copper in conventional long-stroke linear PM machines can be addressed. However, for the existing linear PM vernier (LPMV) machines, the cogging force is relatively high and the force density is relatively low.

In this paper, a novel LPMV machine, which can offer simple structure and high force density, is proposed and analyzed. It employs consequent poles which reduce fringing flux and thus increase flux linkage [19]. In order to further improve force density, a new PM array is proposed in this paper as shown in Fig. 1 together with that of an existing design. It should be noted that the proposed LPMV machine belongs to the class of doubly salient machines with PM arrays inserted in the teeth of the short mover [12]. Similar to flux reversal PM machine [20], the introduction of PMs in the tooth shoes will not significantly
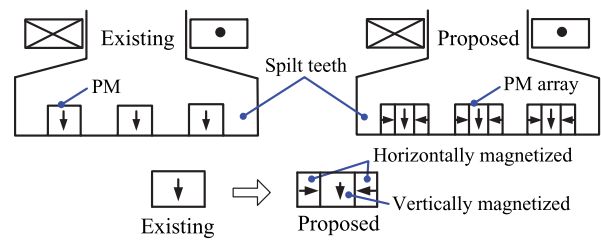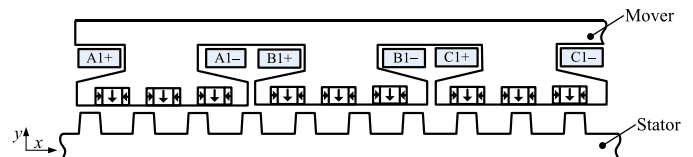
reduce the torque/force density, while improving machine efficiency. The proposed LPMV machine topology enables the use of a salient-pole passive stator without PMs or windings, thus significantly reducing the cost of long-stroke linear PM machines. The novelty of the proposed machine consists of the PM arrays with two magnetized directions, namely horizontally and vertically. This improves the utilization of magnets as all PMs are used to produce the main flux, while the horizontally magnetized PMs reduce fringing leakage flux as compared with its counterparts in [18], hence increasing the thrust force capability.

It is well known that the machine topology significantly affects machine performance such as detent force, back electromotive force (back-EMF), and inductance. The proposed LPMV machine is designed to have high thrust force, low detent force, and low thrust force ripple, and its performance is analyzed by finite-element method (FEM). The merits of the proposed machine are validated by experiments based on a prototype machine.

II. Topology and Operation Principle

A. Topology

Fig. 2 shows the topology of the proposed LPMV machine. The long stator is made of simple iron core with salient teeth so that it offers a low cost and robust structure to generate and transmit thrust force. The mover consists of the iron core with salient teeth wound with three-phase concentrated armature windings and a number of PM arrays inserted in the inner surface of the mover teeth. One PM array has three PMs, whose magnetization directions are illustrated by the arrows in Fig. 2. The vertically magnetized PM is sandwiched between the two horizontally magnetized PMs to reduce PM fringing leakage flux, hence improving air-gap flux density. Since both PMs and armature windings are located on the mover, the proposed machine topologies are very cost-effective for long-stroke linear machines. As can be seen from Fig. 2, every tooth has three PM arrays separated by four spilt teeth.
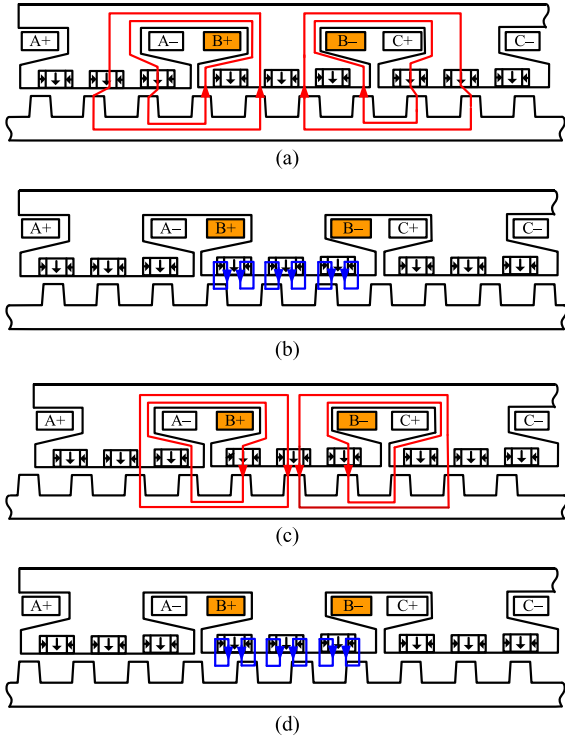
Fig. 3. Operation principle at different mover positions. (a) Position a. (b) Position b. (c) Position c. (d) Position d.

B. Operation Principle

The operation principle of the proposed machine is based on the magnetic field modulation. The two-pole magnetic field produced by the three-phase armature windings on the mover in Fig. 2 is modulated by the 10 stator teeth. This modulation produces nine-pole magnetic field in the air-gap which interacts with the nine-consequent-pole PM field on the mover to produce thrust force. The operation of the machine is further illustrated in Fig. 3 in terms of the back-EMF of Phase B as example, where four typical mover positions are shown. When the relative position of the mover tooth associated with Phase B is aligned with the stator teeth as shown in Fig. 3(a), the Phase B flux linkage is at maximum while its back-EMF is zero. However, the flux linkage becomes zero while the phase back-EMF reaches its positive maximum when the stator is displaced with respect to the mover by a quarter stator tooth pitch as shown in Fig. 3(b). Following a relative stator displacement of a half tooth pitch as shown in Fig. 3(c), the phase flux linkage is at the negative maximum, while the phase back-EMF becomes zero, again. At the mover position as shown in Fig. 3(d) when the stator is displaced relative to the mover by three quarters of the tooth pitch, the phase back-EMF becomes negative maximal.

To further illustrate the operation principle of the proposed machines, the following assumptions are made: the permeability of the stator and mover cores is infinite; the variation of the air-gap magnetic field is only in the x-direction with reference to the coordinate system shown in Fig. 2. Similar to magnetic gears or PM vernier machines, the magnets on the mover of the proposed LPMV machine generate current linkage, commonly known as magneto-motive force. When the y-axis of the mover

co-ordinate system is defined to coincide with the center of one of the PM arrays, the current linkage distribution can be expressed as

$$F(x) = \sum_{n,\text{odd}}^{\infty} F_n \cos\left[np_{\text{PM}} \frac{2\pi x}{l_a} \right]. \quad (1)$$

Due to the slot opening, the value of p_{PM} may not be equal to the number of total PM pole pairs on the mover [17]. The field of the magnets is modulated by the permeance variation of stator teeth expressed as

$$\Lambda(x,t) = \Lambda_0 + \sum_{k=1}^{\infty} \Lambda_k \cos\left[kn_s \frac{2\pi}{l_a}(x - vt - x_0) \right]. \quad (2)$$

The resultant air-gap flux density distribution is given by

$$B(x,t) = F(x)\Lambda(x,t)$$
$$= \sum_{n,\text{odd}}^{\infty} F_n \Lambda_0 \cos\left[np_{\text{PM}} \frac{2\pi x}{l_a} \right] + \sum_{n,\text{odd}}^{\infty} \sum_{k=1}^{\infty} F_n \Lambda_k \cos$$
$$\times \left[np_{\text{PM}} \frac{2\pi x}{l_a} \right] \cos\left[kn_s \frac{2\pi}{l_a}(x - vt - x_0) \right]. \quad (3)$$

It can be rewritten as

$$B(x,t) = F(x)\Lambda(x,t)$$
$$= \sum_{n,\text{odd}}^{\infty} F_n \Lambda_0 \cos\left[np_{\text{PM}} \frac{2\pi x}{l_a} \right] + \frac{1}{2} \sum_{n,\text{odd}}^{\infty} \sum_{k=1}^{\infty} F_n \Lambda_k \cos$$
$$\times \left[\frac{2\pi x}{l_a}(np_{\text{PM}} + kn_s) - \frac{2\pi kn_s(vt + x_0)}{l_a} \right]$$
$$+ \frac{1}{2} \sum_{n,\text{odd}}^{\infty} \sum_{k=1}^{\infty} F_n \Lambda_k \cos\left[\frac{2\pi x}{l_a}(np_{\text{PM}} - kn_s) \right.$$
$$\left. + \frac{2\pi kn_s(vt + x_0)}{l_a} \right]. \quad (4)$$

It can been seen from (4) that the number of pole pairs $P_{n,k}$ of the resultant spatial field distribution is related to the effective PM pole pairs p_{PM} and the number of active stator teeth n_s by

$$P_{n,k} = |np_{\text{PM}} - kn_s|. \quad (5)$$

When $n = 1$ and $k = 1$, the resultant harmonic has the lowest order and hence the largest magnitude. Thus, the pole-pair number of the fundamental component of the air-gap magnetic field produced by the mover magnets and modulated by the stator teeth is

$$P_{1,1} = |p_{\text{PM}} - n_s|. \quad (6)$$

The fundamental component in the second term of (4) associated with $n = 1$ and $k = 1$ represents a traveling waveform with the speed given as follows:

$$v_{1,1} = n_s v / P_{1,1}. \quad (7)$$

In order to produce continuous and smooth thrust force, the traveling waveform of the air-gap magnetic field excited by the
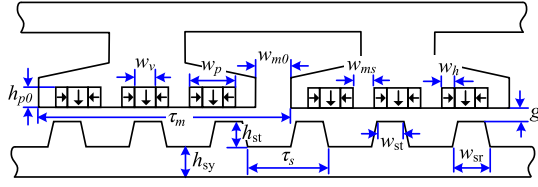
Fig. 4. Definitions of leading machine design parameters.

currents in the armature windings should have the same number of pole-pairs as $P_{1,1}$ and the same speed as the fundamental component of the PM spatial field, thus,

$$v_{1,1} = v_w = \frac{n_s}{n_w}v \qquad (8)$$

$$n_w = P_{1,1} \qquad (9)$$

$$G_r = \frac{n_s}{n_w}. \qquad (10)$$

It follows that the proposed machine has a gearing effect defined by the n_s-to-n_w ratio, and hence yields high force capability.

III. MACHINE DESIGN

The output power of the proposed machine may be estimated by (11) based on commonly used sizing equation of electric machines with due account of magnetic gearing

$$P_{\text{em}} = \frac{\sqrt{2}}{2n_a}mB_{e\delta}l_ml_ac_sk_dA_svG_r. \qquad (11)$$

It is seen from (5) that magnetic gear ratio G_r is a key design parameter for the proposed machine. This is because it influences the rate of change of flux linkage with respect to mover displacement. The other leading design parameters of the basic module of the proposed machine are defined in Fig. 4. The choice of these parameters could be guided by the sizing equation and should follow a number of basic rules. First, the permeance variation should be maximized and hence the permeance, when the mover PM arrays and the stator teeth are unaligned, should be minimized. Thus, the mover PM arrays width and the stator slot pitch should satisfy the relationship

$$w_v + 2 \cdot w_h < \tau_s. \qquad (12)$$

Second, the machine thrust force is mainly contributed by the magnetic field of the vertically magnetized PMs. In addition, the proposed machine should have sinusoidal back-EMF, suitable for brushless ac (BLAC) operation. This implies that the vertically magnetized PM width should be larger than the horizontally magnetized one, namely,

$$w_h \leq w_v. \qquad (13)$$

For the proposed machine, the ratio of the PM array significantly affects its electromagnetic performance. So, it is important to identify this ratio. The PM array optimization is based on a fixed spilt slot width w_p as shown in Fig. 4. Other design parameters are determined by considering their influence on the back-EMF and other performance indicators, such as detent force and inductances. For example, the air-gap length
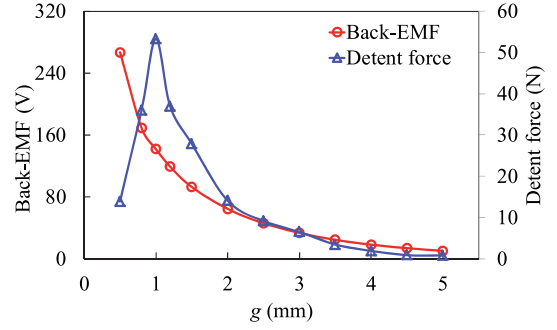

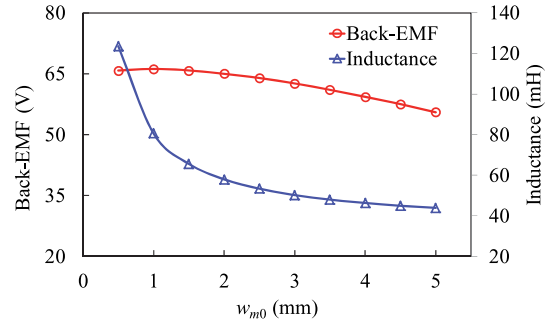Fig. 5. Variation in back-EMF and detent force with respect to g.

Fig. 6. Variation in back-EMF and inductance with respect to w_{m0}.

g, whose influence on the back-EMF and detent force is shown in Fig. 5, is selected to be 2 mm. The back-EMF and inductance variation with the mover slot opening width w_{m0} is shown in Fig. 6. Obviously, as the slot opening width increases, the back-EMF and the inductance of the machine gradually decreases. Since a low inductance is conducive to high power factor, w_{m0} is designed to be 2 mm. The number of conductor in each phase is 200, the mover spilt slot width w_p is 9 mm, and the mover width l_m (in the z-direction) is 120 mm.

The other parameters to be designed include two-dimensional ratios against the mover spilt slot width w_p. These are the ratio of the vertically magnetized PM width to the mover spilt slot width k_v and the ratio of the horizontally magnetized PM width to the mover spilt slot width k_h defined as follows:

$$k_v = w_v/w_p \qquad (14)$$

$$k_h = w_h/w_p. \qquad (15)$$

According to (13), k_v should be larger than k_h. When the mover spilt teeth width w_{ms} and spilt slot width w_p are fixed, the two ratios are related by

$$k_v + 2 \cdot k_h = 1. \qquad (16)$$

Therefore, only one variable k_h has to be optimized. The initial values of horizontally magnetized PMs width w_h and the corresponding ratio k_h are 1.5 mm and 1/6, respectively. Fig. 7 shows the variation in the fundamental peak back-EMF with the horizontally magnetized PM ratio k_h. It is evident that there is an optimal k_h which yields the maximum EMF. The optimal value of k_h is 0.22, which means that the horizontally magnetized PM width is 2 mm. The corresponding k_v is 0.56, and the width of vertically magnetized PM is 5 mm, which satisfies (13).
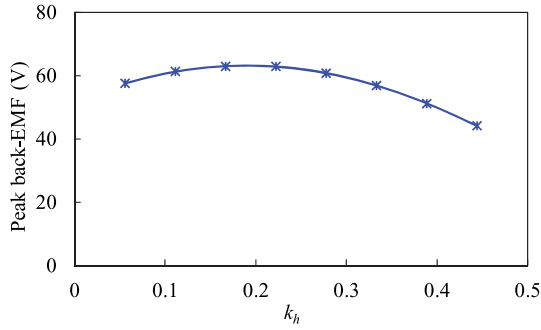
Fig. 7. Variations in back-EMF with respect to k_h.

Other variables that have significant influence on back-EMF or thrust force capability are investigated. The stator tooth tip width ratio k_p given in (17), the PM width ratio k_{PM} in (18), and the magnet thickness h_{P0} are three main factors

$$k_p = w_p/w_{st} \qquad (17)$$
$$k_{PM} = w_p/\tau_m. \qquad (18)$$

Fig. 8 shows the variations of fundamental back-EMF of the proposed machine with the three design variables. It is seen in Fig. 8(a) that as the stator tooth tip width ratio k_p increases, the amplitude of the peak back-EMF gradually increases, and then reduces. The appropriate value for k_p is 1.9 and the stator tooth tip width is 4.7 mm. Fig. 8(b) reveals the relationship of the peak back-EMF with the PMs width ratio k_{PM}. It can be seen that the back-EMF gradually increases initially and then rapidly declines. Thus, k_{PM} is selected to be 0.18. The influence of magnet thickness h_{P0}, which is a key parameter for not only the back-EMF but also the machine cost, is illustrated in Fig. 8(c). It can be seen that as the magnet thickness increases, the back-EMF increases first rapidly, then gradually. The magnet thickness is selected to be 5 mm as a tradeoff with the cost. The detailed design parameters for a prototype machine are listed in Table I, and the resultant performance and loss components at the rated operation are listed in Table II. It can be seen that the copper loss is the main loss component and the machine efficiency at the rated operation is 87.3%, which is nearly 10% higher than that of the existing machine reported in [18]. It should be noted that the thrust force density of 0.15 MN/m3 is lower than those of typical linear PM machines reported in literature. However, this force density is achieved with 2.0-mm air-gap length and a cost-effective machine topology for long-stroke applications.

While the influences of the leading design parameters on the machine performance and cost have been analyzed and their values are selected, comprehensive optimization will further improve the machine performance. This topic is beyond the scope of this paper.

IV. PERFORMANCE EVALUATION

A. Open-Circuit Field Distributions

The flux characteristics of the proposed machine are analyzed by FEM, and compared with that of the existing one shown in Fig. 1. It should be noted that they are designed based
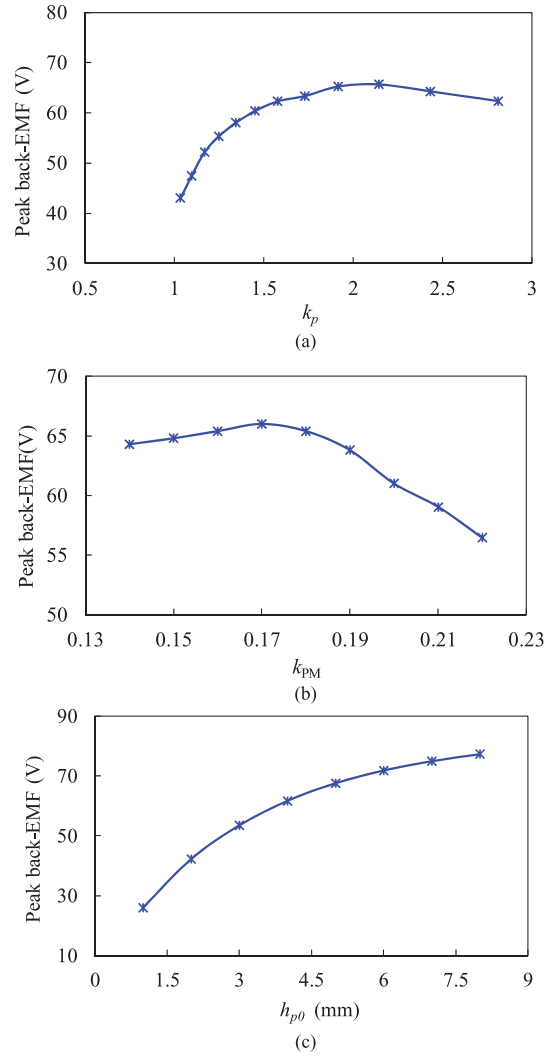

Fig. 8. Variations in peak back-EMF with respect to parameters. (a) k_p. (b) k_{PM}. (c) h_{P0}.

on the same size and electrical loading. Fig. 9 compares their magnetic field distributions at no-load and both are plotted in the same range of vector magnetic potentials. It can be seen that the existing machine suffers from significant flux leakage and saturation in the interface regions between the magnets and the core. It can also be observed that the use of the horizontally magnetized PMs has significantly reduced the leakage flux of the proposed machines as compared with its counterpart.

Furthermore, Fig. 10 compares the air-gap magnetic flux density waveforms and the harmonic spectra of the two design variants at no-load. It can be seen that the proposed machine has higher flux density than the existing one. For the proposed machine, there are a number of space harmonics resulting from the modulation of magnetic field by the stator teeth and the spilt teeth on the mover. The most significant harmonics include the 2nd, 6th, 12th, 18th, and 24th. The number of the actual PM pole pairs over one mover electric period within 14.7 mm is 18, which corresponds to the 18th harmonic of the highest amplitude. This implies that the effective number of pole pairs p_{PM} is 18. In addition, the copper loss and iron loss in the stator, the iron loss in the mover, and the eddy current loss in

TABLE I
DESIGN SPECIFICATIONS OF PROTOTYPE MACHINE

Mover width, l_m (mm)	120
Mover pole pitch, τ_m (mm)	49
Mover slot opening, w_{m0} (mm)	2
Mover splittooth width, w_{ms} (mm)	5
PM thickness, h_{P0} (mm)	5
Vertically magnetized PM width, w_v (mm)	5
Horizontally magnetized PM width, w_h (mm)	2
Stator pole pitch, τ_s (mm)	14.7
Stator tooth tip, w_{st} (mm)	5.2
Stator tooth root, w_{sr} (mm)	5.7
Stator tooth height, h_{st} (mm)	8
Number of slot/pitch	18/20
Air-gap length, g (mm)	2
Magnet material	NdFe35
Magnet remanence, B_i (T)	1.2
Current density, J (A/mm^2)	3.5
Copper mass, M_{cu} (kg)	1.8

TABLE II
MACHINE LOSS

Rated speed, v (m/s)	1.5
Rated power (W)	480
Force density (N/m^3)	1.5×10^5
Rated voltage (V)	270
Rated current (A)	3.5
Copper loss (W)	48.6
Mover iron loss (W)	11.6
Stator iron loss (W)	6
Magnets eddy loss (W)	0.8
Additional losses (W)	2
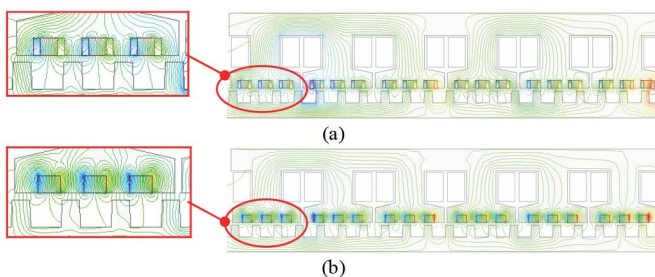
Fig. 9. Field distributions at no-load. (a) Proposed. (b) Existing.

the mover magnets at the rated speed and current have also be quantified and listed in Table II. It can be noted that the iron and copper losses are significantly higher than the eddy current loss.

B. Flux Linkage, Back-EMF, and Inductance

The FEM-predicted PM flux linkages are shown in Fig. 11. Each phase consists of two coils denoted as 1 and 2, and connected in series. It is seen that the flux linkages in the three phases are unbalanced, and in particular the flux linkage in coil
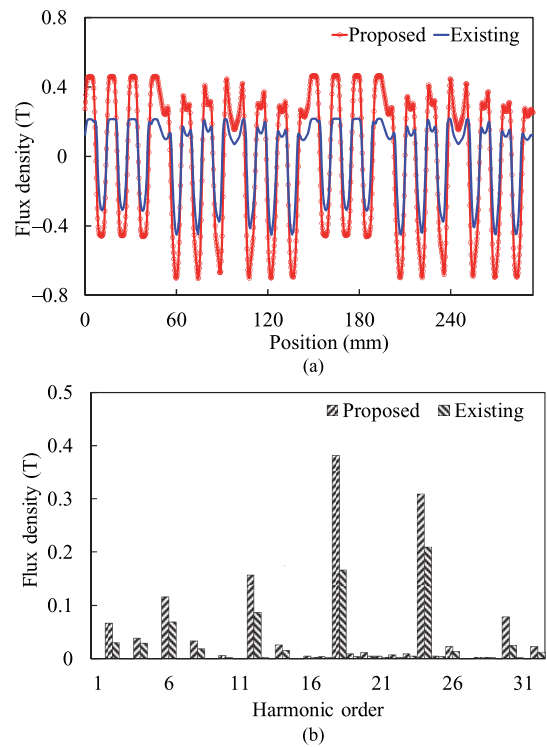
Fig. 10. Air-gap flux density distributions of both machines. (a) Waveform. (b) Harmonic spectra.
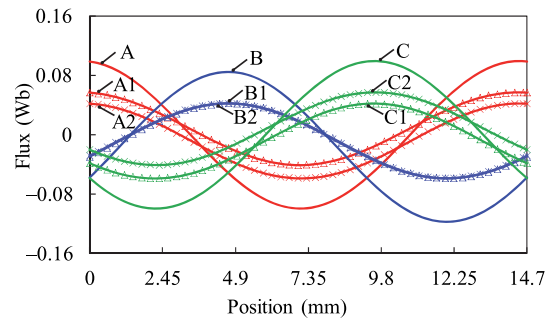
Fig. 11. PM flux linkages.

C2 of phase C comprises a dc offset due to the end effects [21], [22]. Similar phenomenon is observed in the coil flux-linkages of phase A. Furthermore, the flux linkage of each phase is asymmetry with the negative peak being larger than the positive. This is caused by the consequent poles in the proposed LPMV machine.

The phase back-EMF E can be expressed as

$$E = \frac{d\psi}{dt} = \frac{d\psi}{dx} v. \tag{19}$$

Therefore, the back-EMF is only related to the rate of change in the flux linkage. For the proposed machine, although its phase flux linkages are asymmetry as shown in Fig. 11, the rate of change of the phase flux linkages is sinusoidal. Hence, its back-EMFs are also sinusoidal and symmetrical as shown in Fig. 12.
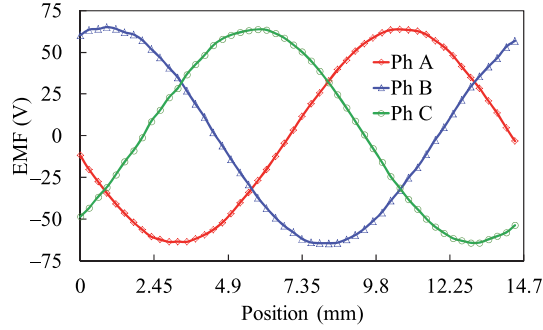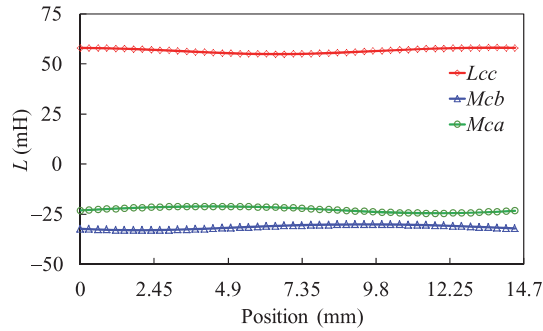
Fig. 12. Back-EMFs at mover speed of 1.5 m/s.

Fig. 13. Comparison of self- and mutual-inductances.

The self- and mutual-inductances of each phase can also be predicted by FEM. For example, the self- and mutual inductances of phase C are calculated as

$$
\begin{cases}
L_{cc} = \frac{\psi_C(I_a=I_b=0, I_c=I) - \psi_C(I_a=I_b=I_c=0)}{I} \\
L_{ca} = \frac{\psi_A(I_a=I_b=0, I_c=I) - \psi_C(I_a=I_b=I_c=0)}{I} \\
L_{cb} = \frac{\psi_B(I_a=I_b=0, I_c=I) - \psi_C(I_a=I_b=I_c=0)}{I}.
\end{cases}
\tag{20}
$$

Fig. 13 compares the predicted variations of phase C self- and mutual inductances of the proposed machine. They can be approximated by

$$
\begin{cases}
L_{cc} = L_0 + L_{max} \sin \frac{2\pi}{\tau_s}(x + x_1) \\
M_{ca} = M_0 + M_{max} \sin \frac{2\pi}{\tau_s}(x + x_2) \\
M_{cb} = M_0 + M_{max} \sin \frac{2\pi}{\tau_s}(x + x_3).
\end{cases}
\tag{21}
$$

Consequently, the thrust force ripple caused by the fluctuating inductances of the proposed machine can be predicted, which will be discussed in the next section.

C. Detent Force and Thrust Force

The electromagnetic force of a given phase may be expressed as

$$
F = i\frac{d\psi_{PM}}{dx} + \frac{1}{2}i^2\frac{dL}{dx} + \frac{d}{dx}\left(\frac{1}{2}i^2 L\right).
\tag{22}
$$

The first term in (22) is the force produced by the PM field; the second and third terms are the forces caused by the position-dependent inductances. Thus, the inductance variations with mover position in the proposed machine may give rise to fluctuating force. This can be analyzed by induced voltages in each phase. For example, the induced voltage in phase C can be written as (23), shown at the bottom of the page.

It should be noted that, in (23), the first term is produced by the PM flux linkage, while the second- and third-term components are produced by current and inductance changes. If the d-axis current is controlled to be 0, i.e., the applied current is in phase with the back-EMF, the fluctuating force contributed by phase C can be written as

$$
\begin{aligned}
F_{rC} &= (L_0 - M_0)i_c\frac{di_c}{dx}v + i_c\frac{d\left(L_{max}\sin\frac{2\pi}{\tau_s}(x+x_1)\right)i_c}{dx}v \\
&+ i_c\frac{d\left(M_{max}\sin\frac{2\pi}{\tau_s}(x+x_2)i_a + M_{max}\sin\frac{2\pi}{\tau_s}(x+x_3)i_b\right)}{dx}v.
\end{aligned}
\tag{24}
$$

The fluctuating force generated by the three phases can be calculated as

$$
F_r = F_{rA} + F_{rB} + F_{rC}.
\tag{25}
$$

In addition, detent force caused by both the end effect and the slotting effect also exists in the proposed machine. By employing the method in [23], the detent force components due to slotting and end effect of the proposed machine can be segregated, as shown in Fig. 14. It can be seen that the peak-to-peak detent force is 34.7 N. The end effect detent force is much smaller than the slotting effect force and can be neglected.

For the proposed LPMV machine, the output thrust force can be written as

$$
F_{out} = F_{ele} + F_{detent}.
\tag{26}
$$

The electromagnetic force F_{ele} in (26) contains the fluctuating force which can be calculated by (25). Fig. 15 compares the fluctuating force of the proposed LPMV machine calculated

$$
\begin{aligned}
E_c &= \frac{d\psi}{dx}v = \frac{d(L_{cc}i_c + M_{ca}i_a + M_{cb}i_b + \psi_{PM})}{dx}v \\
&= \frac{d\left(L_0 + L_{max}\sin\frac{2\pi}{\tau_s}(x+x_1)\right)i_c + \left(M_0 + M_{max}\sin\frac{2\pi}{\tau_s}(x+x_2)i_a\right)}{dx}v + \frac{d\left(\left(M_0 + M_{max}\sin\frac{2\pi}{\tau_s}(x+x_3)\right)i_b + \psi_{PM}\right)}{dx}v \\
&= \frac{d\psi_{PM}}{dx}v + (L_0 - M_0)\frac{di_c}{dx}v + \frac{d\left(\left(L_{max}\sin\frac{2\pi}{\tau_s}(x+x_1)\right)i_c + M_{max}\sin\frac{2\pi}{\tau_s}(x+x_2)i_a + M_{max}\sin\frac{2\pi}{\tau_s}(x+x_3)i_b\right)}{dx}v
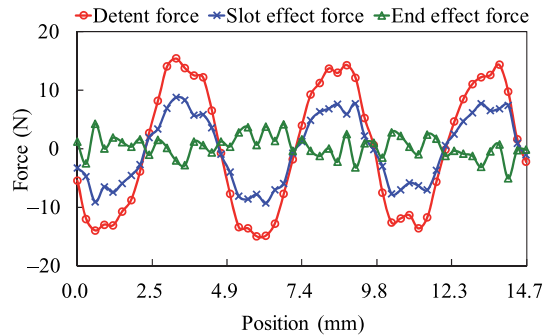\end{aligned}
\tag{23}
$$

Fig. 14. Variations in detent force and its slotting effect and end effect components with mover position.
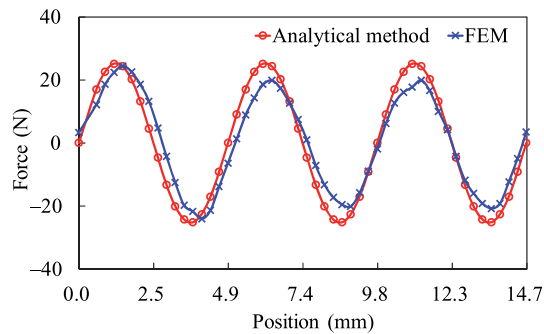

Fig. 15. Comparison of FE and analytically predicted fluctuating force variations with mover position.
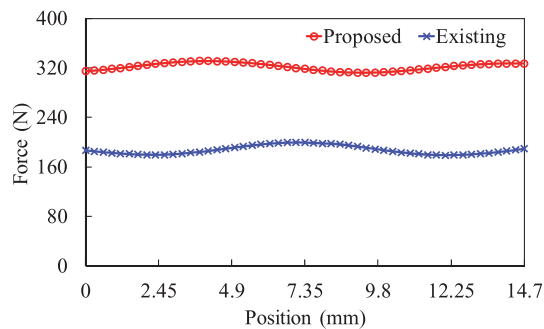

Fig. 16. Comparison of thrust force variations with mover position.

by FEM and by the analytical method given by (24) and (25). Good agreement between the two results is observed. It is worth noting that the detent force and the fluctuating force are in opposite phase, and hence, the resultant force ripple of the proposed machine is much reduced.

Fig. 16 compares the thrust force of the proposed machine with that of the existing one, when both machines are excited by three-phase sinusoidal current of 5 A. It can be seen that the proposed machine has much higher force capability than the existing one. The thrust force performance of the proposed LPMV machine can be assessed by the thrust force ripple factor defined as follows:

$$K_F = \frac{F_{\max} - F_{\min}}{F_{av}} \times 100\%. \qquad (27)$$

The peak-to-peak force $(F_{\max} - F_{\min})$ is 17 N, which is much lower than the peak-to-peak detent force.
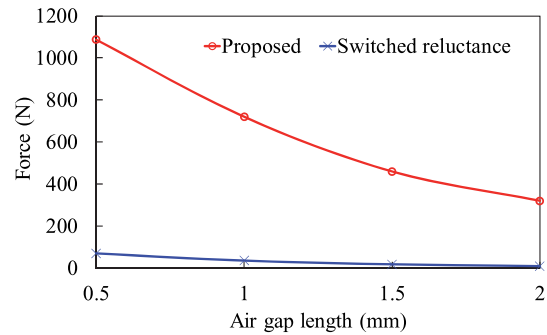

Fig. 17. Comparison of thrust forces of proposed and switched reluctance machines.
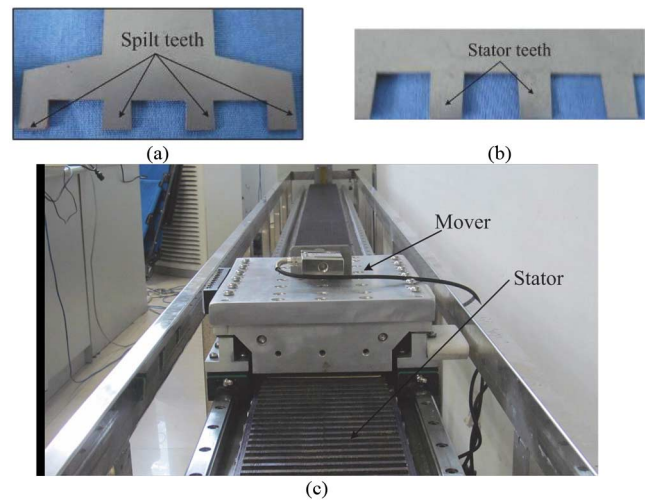

Fig. 18. Prototype of the proposed LPMV machine. (a) Mover laminated segment. (b) Stator laminated segment. (c) Machine.

While linear synchronous reluctance and switched reluctance machines may be of low cost, they have much lower force density, lower efficiency, and lower power factor compared with linear PM counterparts. They also require small air-gap which is not possible in some applications such as urban rail transit system. By way of example, a linear switched reluctance machine [24] is designed based on the same size and electrical loading as those of the proposed machine. Fig. 17 compares the force variations with air-gap length of the two machines. As can be seen, when the air-gap length is 0.5 mm, the thrust force of the linear switched reluctance machine is 70 N, while that of the proposed machine is 1087 N. As the air-gap length increases, the thrust force of the switched reluctance machine diminishes. Therefore, it will not be suitable for rail transit application which requires a large air-gap. In fact, the proposed machine has the advantage of high force density and high efficiency of linear PM machines, while the use of PMs and copper is minimized for long-stroke application. It is also possible to use ferrite magnets for further cost reduction [25].

V. EXPERIMENTAL VERIFICATION

A prototype LPMV machine, as shown in Fig. 18, has been designed and built to validate the theoretical analysis. The experiment platform is built, in which a linear encoder is used
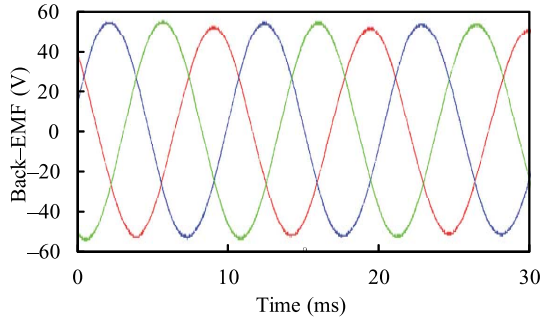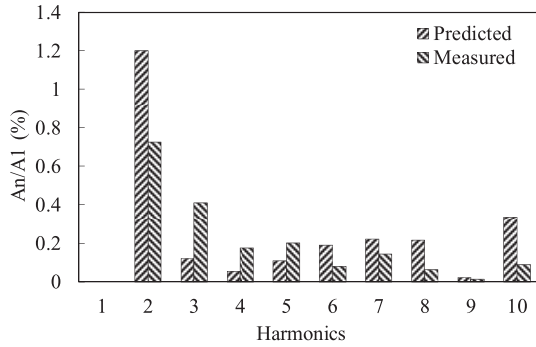
Fig. 19. Measured back-EMF waveforms at 1.5 m/s.

Fig. 20. Comparison of predicted and simulated harmonic spectra (base value $= 54\,\mathrm{V}$, speed $= 1.5\,\mathrm{m/s}$).
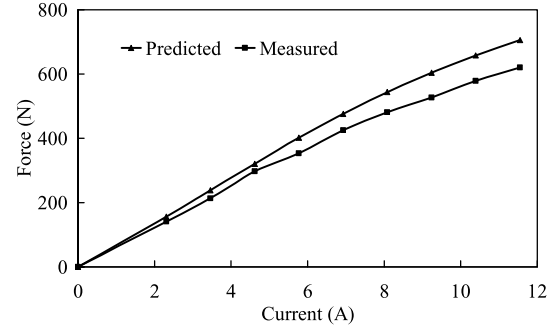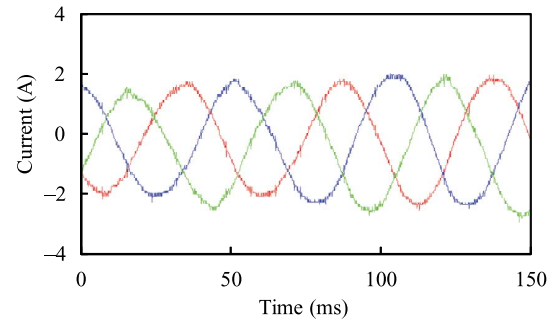

Fig. 21. Predicted and Measured thrust force variations with current.

Fig. 22. Measured currents at 0.3 m/s and 150 N.

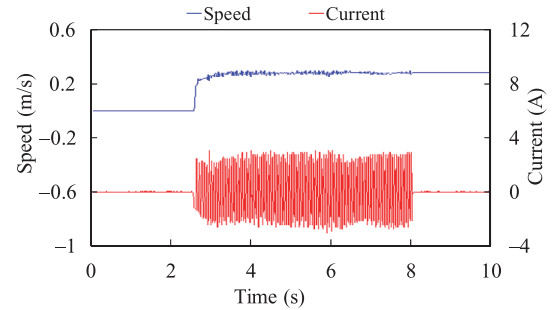Fig. 23. Measured responses of mover speed and phase current.

to measure the mover position and speed. Voltage and current sensors with appropriate signal conditioning circuitry are used to measure the phase voltage and current, and a force sensor is employed to measure the thrust force. The prototype machine is controlled by a digital signal processing unit, TMS320F2812, through a three-phase integrated power module (IPM).

The three-phase back-EMFs of the prototyped machine at the mover speed of 1.5 m/s are measured, as shown in Fig. 19. It is evident that the proposed LPMV machine has sinusoidal and symmetric back-EMFs, which agrees with the predictions in Fig. 12. The insignificant discrepancies between the experimental and simulated results mainly result from the end effect and manufacture tolerance. Furthermore, by applying spectral analysis to the predicted and the measured back-EMF waveforms, the corresponding fundamental components and harmonic spectra can be deduced. The harmonic spectra are normalized to the measured fundamental component as shown in Fig. 20. It should be noted that An $(n = 1, 2, 3, \ldots, 10)$ is the magnitude of the nth-order harmonic, and A1 is the magnitude of the fundamental component. It can be observed that the total harmonic distortion of the measured back-EMF waveform is less than 1.5%, in which the relatively large third-order harmonic actually does not contribute to production of force ripple. Fig. 21 compares the predicted and the measured locked thrust force variations with current when phase A is aligned with the d-axis. It can be seen that the predicted forces agree reasonably well with the measurements. The discrepancies between the predicted and the measured results are mainly caused by the friction, the end effects, and the manufacture tolerance. Moreover, the measured steady-state current waveforms when the machine operates in the BLAC mode at 0.3 m/s and 150 N

are shown in Fig. 22. Furthermore, the dynamic performance of the proposed LPMV machine drive is evaluated. The measured responses of the mover speed and phase current to a step demand of 0.3 m/s are given in Fig. 23, showing that the proposed motor has a satisfactory dynamic performance. It should be mentioned that the significant friction force and nonuniform air-gap of the prototype affect the operation performance. Hence, advanced control strategies for the prototype will be investigated in future work.

VI. CONCLUSION

In this paper, a novel LPMV machine that employs magnet arrays with appropriate magnetization directions has been described. The salient feature of the proposed machine is that both the three-phase armature windings and PMs are integrated in a short mover, while the stator is made of toothed lamination. Thus, the proposed machine topology is particularly suited for long-stroke applications. It has been shown that the proposed

machine exhibits high force density with relatively large air-gap necessary for the targeted application in urban rail transit systems. It has also been found the thrust force ripple of the proposed machine is quite lower since the detent force and the fluctuating force due to reluctance variation are in opposite phase. The merits and performance of the proposed machine have been validated by the measurements on the prototype machine and drive.

REFERENCES

[1] R. Cao, C. Mi, and M. Cheng, "Quantitative comparison of flux-switching permanent-magnet motors with interior permanent magnet motor for EV, HEV, and PHEV applications," *IEEE Trans. Magn.*, vol. 48, no. 8, pp. 2374–2384, Aug. 2012.

[2] X. Chen and J. Wang, "A high-fidelity and computationally efficient model for interior permanent-magnet machines considering the magnetic saturation, spatial harmonics, and iron loss effect," *IEEE Trans. Ind. Electron.*, vol. 62, no. 7, pp. 4044–4055, Jul. 2015.

[3] R. Cao, M. Cheng, and B. Zhang, "Speed control of complementary and modular linear flux-switching permanent-magnet motor," *IEEE Trans. Ind. Electron.*, vol. 62, no. 7, pp. 4056–4064, Jul. 2015.

[4] J. Ji, W. Zhao, Z. Fang, J. Zhao, and J. Zhu, "A novel linear permanent-magnet vernier machine with improved force performance," *IEEE Trans. Magn.*, vol. 51, no. 8, Aug. 2015, Art. ID. 8106710.

[5] N. Niguchi and K. Hirata, "Cogging torque analysis of magnetic gear," *IEEE Trans. Ind. Electron.*, vol. 59, no. 5, pp. 2189–2197, May 2012.

[6] T. Lubin, S. Mezani, and A. Rezzoug, "Experimental and theoretical analyses of axial magnetic coupling under steady-state and transient operations," *IEEE Trans. Ind. Electron.*, vol. 61, no. 8, pp. 4356–4365, Aug. 2014.

[7] L. Sun, M. Cheng, and H. Jia, "Analysis of a novel magnetic-geared dual-rotor motor with complementary structure," *IEEE Trans. Ind. Electron.*, vol. 62, no. 11, pp. 6737–6747, Nov. 2015.

[8] S. Niu, S. Ho, and W. Fu, "Performance analysis of a novel magnetic-geared tubular linear permanent magnet machine," *IEEE Trans. Magn.*, vol. 47, no. 10, pp. 3598–3601, Oct. 2011.

[9] W. Li, K. Chau, C. Liu, S. Gao, and D. Wu, "Analysis of tooth-tip flux leakage in surface-mounted permanent magnet linear vernier machines," *IEEE Trans. Magn.*, vol. 49, no. 7, pp. 3949–3952, Jul. 2013.

[10] S. L. Ho, S. Niu, and W. N. Fu, "Design and comparison of vernier permanent magnet machines," *IEEE Trans. Magn.*, vol. 47, no. 10, pp. 3280–3283, Oct. 2011.

[11] M. Wang, L. Li, and D. Pan, "Detent force compensation for PMLSM systems based on structural design and control method combination," *IEEE Trans. Ind. Electron.*, vol. 62, no. 11, pp. 6845–6854, Nov. 2015.

[12] M. Cheng, W. Hua, J. Zhang, and W. Zhao, "Overview of stator-permanent magnet brushless machines," *IEEE Trans. Ind. Electron.*, vol. 58, no. 11, pp. 5087–5101, Nov. 2011.

[13] W. Zhao, M. Cheng, K. T. Chau, R. Cao, and J. Ji, "Remedial injected-harmonic-current operation of redundant flux-switching permanent-magnet motor drives," *IEEE Trans. Ind. Electron.*, vol. 60, no. 1, pp. 151–159, Jan. 2013.

[14] Z. Wu and Z. Q. Zhu, "Analysis of air-gap field modulation and magnetic gearing effects in switched flux permanent magnet machines," *IEEE Trans. Magn.*, vol. 51, no. 5, May 2015, Art. ID. 8105012.

[15] M. Cheng, K. T. Chau, and C. C. Chan, "Design and analysis of a new doubly salient permanent magnet motor," *IEEE Trans. Magn.*, vol. 37, no. 4, pp. 3012–3020, Jul. 2001.

[16] S. Zhu, M. Cheng, J. Dong, and J. Du, "Core loss analysis and calculation of stator permanent-magnet machine considering DC-biased magnetic induction," *IEEE Trans. Ind. Electron.*, vol. 61, no. 10, pp. 5203–5212, Oct. 2014.

[17] Y. Du *et al.*, "Comparison of linear primary permanent magnet vernier machine and linear vernier hybrid machine," *IEEE Trans. Magn.*, vol. 50, no. 11, Nov. 2014, Art. ID. 8202604.

[18] Y. Du *et al.*, "Design and analysis of linear stator permanent magnet vernier machines," *IEEE Trans. Magn.*, vol. 47, no. 10, pp. 4219–4222, Oct. 2011.

[19] S. Chung, J. Kim, B. Woo, D. Hong, J. Lee, and D. Koo, "A novel design of modular three-phase permanent magnet vernier machine with consequent pole rotor," *IEEE Trans. Magn.*, vol. 47, no. 10, pp. 4215–4218, Oct. 2011.

[20] I. Boldea, J. Zhang, and S. A. Nasar, "Theoretical characterization of flux reversal machine in low-speed servo drives-the pole-PM configuration," *IEEE Trans. Ind. Appl.*, vol. 38, no. 6, pp. 1549–1557, Nov./Dec. 2002.

[21] T. Yang, L. Zhou, and L. Li, "Influence of design parameters on end effect in long primary double-sided linear induction motor," *IEEE Trans. Plasma Sci.*, vol. 39, no. 1, pp. 192–197, Jan. 2011.

[22] E. Amiri and E. Mendrela, "A novel equivalent circuit model of linear induction motors considering static and dynamic end effects," *IEEE Trans. Magn.*, vol. 50, no. 3, Mar. 2014, Art. ID. 8200409.

[23] C. Wang and J. Shen, "A method to segregate detent force components in permanent-magnet flux-switching linear machines," *IEEE Trans. Magn.*, vol. 48, no. 5, pp. 1948–1955, May 2012.

[24] J. G. Amoros and P. Andrada, "Sensitivity analysis of geometrical parameters on a double-sided linear switched reluctance motor," *IEEE Trans. Ind. Electron.*, vol. 57, no. 1, pp. 311–319, Jan. 2010.

[25] I. Boldea, L. N. Tutelea, L. Parsa, and D. Dorrell, "Automotive electric propulsion systems with reduced or no permanent magnets: An overview," *IEEE Trans. Ind. Electron.*, vol. 61, no. 10, pp. 5696–5711, Oct. 2014.

Wenxiang Zhao (M'08–SM'14) received the B.Sc. and M.Sc. degrees from Jiangsu University, Zhenjiang, China, in 1999 and 2003, respectively, and the Ph.D. degree from Southeast University, Nanjing, China, in 2010, all in electrical engineering.

He has been with Jiangsu University since 2003, where he is currently a Professor with the School of Electrical Information Engineering. From 2008 to 2009, he was a Research Assistant with the Department of Electrical and Electronic Engineering, University of Hong Kong, Pok Fu Lam, Hong Kong. From 2013 to 2014, he was a Visiting Professor with the Department of Electronic and Electrical Engineering, the University of Sheffield, Sheffield, U.K. He has authored or coauthored over 130 technical papers. His research interests include electric machine design, modeling, fault analysis, and intelligent control.

Junqiang Zheng received the B.Sc. degree in electrical engineering from Jiangsu University, Zhenjiang, China, in 2014, where he is currently working toward the Ph.D. degree in electrical engineering.

His research interests include machine design and electromagnetic field computation.

Jiabin Wang (SM'03) received the B.Eng. and M.Eng. degrees from Jiangsu University of Science and Technology, Zhenjiang, China, in 1982 and 1986, respectively, and the Ph.D. degree from the University of East London, London, U.K., in 1996, all in electrical and electronic engineering.

Currently, he is a Professor with the Department of Electrical Engineering, the University of Sheffield, Sheffield, U.K. From 1986 to 1991, he was with the Department of Electrical Engineering, Jiangsu University of Science and Technology, where he was appointed as a Lecturer in 1987 and an Associate Professor in 1990. He was a Postdoctoral Research Associate with The University of Sheffield from 1996 to 1997, and a Senior Lecturer with the University of East London from 1998 to 2001. His research interests include motion control and electromechanical energy conversion to electric drives for applications in automotive, renewable energy, household appliances, and aerospace sectors.

Dr. Wang is a Fellow of the Institution of Engineering and Technology, U.K.

Guohai Liu (SM'15) received the B.Sc. degree from Jiangsu University, Zhenjiang, China, in 1985, and the M.Sc. and Ph.D. degrees from Southeast University, Nanjing, China, in 1988 and 2002, respectively, all in electrical engineering and control engineering.

Since 1988, he has been with Jiangsu University, where he is currently a Professor, and the Dean of the School of Electrical Information Engineering. He has authored or coauthored over 150 technical papers and four textbooks, and holds 15 patents. His research interests include electrical machines, motor drives for electric vehicles, and intelligent control.

Zhuoya Fang received the B.Sc. and M.Sc. degrees in electrical engineering from Jiangsu University, Zhenjiang, China, in 2012 and 2015, respectively.

She is currently with the Basic Engineering Training Center, Jiangsu University, Zhenjiang, China. Her research interests include design and analysis of linear permanent-magnet machines.

Jianxing Zhao received the B.Sc. degree from Southwest University for Nationalities, Chengdu, China, and the M.Sc. degree from Jiangsu University, Zhenjiang, China, in 2011 and 2014, respectively, both in electrical engineering.

He is currently with the the China Shipbuilding Industry Corporation, Shanghai, China. His research interests include design and control of permanent-magnet machines.